BATTERIES

# Strong and brittle lithium dendrites

Qing Ai[1]†, Boyu Zhang[1]†, Xing Liu[2,3]†, Bongki Shin[1], Wenhua Guo[4], Guanhui Gao[1], Lihong Zhao[5], Xintong Weng[1], Qiyi Fang[1], Tianshu Zhai[1], Doug Steinbach[1], Yifan Zhu[1], Yifeng Liu[1], Fan Wang[1], Xiaoyin Tian[1], Hua Guo[1]*, Youtian Zhang[1], Xuan Zhao[6,7], Yimo Han[1], Ming Tang[1], Yan Yao[5]*, Ting Zhu[2]*, Huajian Gao[8,9]*‡, Jun Lou[1,10]*

The growth and penetration of lithium dendrites through electrolytes and separators remain key challenges to realizing high–energy density lithium-metal batteries. Using mechanically strong electrolytes and separators has been considered a promising strategy based on the commonly believed softness of lithium. However, dendrite formation persists in stiff solid electrolytes, suggesting distinct mechanical behaviors. We measured the mechanical properties of individual lithium dendrites using an air-free protocol. We found that lithium dendrites are unexpectedly strong and brittle, with fracture stress greater than ~150 megapascals, unlike the ductile bulk metal. Cryo–transmission electron microscopy and mechanical modeling showed that this behavior arises from solid electrolyte interface constraints and nanoscale strengthening. These findings provide alternative mechanisms for dendrite penetration and dead lithium formation as well as guidance for design strategies for lithium-metal batteries.

Lithium (Li)–metal anodes offer the highest specific capacity (3860 mAh $g^{-1}$) and the lowest electrochemical potential (−3.040 V versus standard hydrogen electrode) among all anode materials (*1*, *2*). However, using Li-metal anodes in the next-generation of Li-ion and "beyond–Li-ion" batteries poses safety challenges. During the charging and discharging of batteries with liquid electrolytes, dendritic Li forms and penetrates separators, leading to internal short circuit or explosion (*2*–*4*). Monroe and Newman proposed that a solid electrolyte (SE) with a shear modulus twice that of Li metal can prevent dendrite growth (*5*), leading to the belief that high-modulus inorganic SEs can suppress dendrite formation and growth. However, recent studies show that Li dendrites can still break stiff SEs, including high-modulus oxides, such as garnet-type lithium lanthanum zirconium oxide (LLZO) (*6*, *7*). These results raise a notable question: Given that Li metal is soft and deformable, how can it break much harder SEs (*8*–*10*)? To address this question, it is essential to quantify the mechanical properties of Li dendrites. Recent studies have shown that Li metal exhibits high yield stresses at smaller scales, suggesting that strength increases as size decreases (*11*–*13*). However, owing to the complex electrochemical conditions inside batteries, Li dendrites may behave differently from pure Li (*14*). Therefore, it is critical to measure the mechanical properties of Li dendrites grown within batteries, as this information is key to improving Li-metal battery performance and predicting failure modes.

We developed an air-free method to measure the tensile mechanical properties of as-grown Li dendrites that are several hundred nanometers in width. Using a nanomanipulator in a scanning electron microscope (SEM), we transferred Li dendrites grown in a coin cell to a customized nanomechanical testing device and then performed in situ tensile tests. The entire process was conducted in a protective environment to prevent chemical degradation of the Li dendrites. Both the tensile stress–strain curves and fracture observations indicate that Li dendrites are brittle, fracturing at a tensile stress greater than ~150 MPa without visible plastic deformation, unlike bulk Li metal, which yields at ~0.6 MPa. Cryo–transmission electron microscopy (cryo-TEM) images show that each Li dendrite has a Li core covered by a ~15-nm-thick solid electrolyte interface (SEI). Finite element modeling shows that the experimentally observed high strength and brittle fracture behavior of the as-grown Li dendrite stems from the high yield stress of the Li core, estimated to exceed 115 MPa. Dislocation mechanics analysis attributes this elevated yield stress to the suppression of plastic deformation caused by the limited dislocation sources in the Li core together with the surface constraint by the SEI layer. Additionally, dislocation pile-up against the Li-SEI interface further increases resistance to yielding, resulting in the high tensile strength measured in experiments. These combined experimental and theoretical findings provide insights into the failure mechanisms of Li dendrites, which are critical for the safe operation of Li-metal batteries.

## In situ tensile test of Li dendrites

Quantitative mechanical testing of Li dendrites is challenging owing to their high chemical reactivity, sensitivity to air or moisture, handling difficulties, and electron beam (e-beam) effects inside an SEM. To address these issues, we developed an air-free protocol for transferring and testing Li dendrites. Figure 1, A and B, illustrates the preparation of an Li dendrite sample within a coin cell setup. A copper (Cu) TEM grid (400 mesh) served as the current collector to support Li dendrite growth and facilitate sample transfer using a nanomanipulator inside an SEM. Li metal was used as the counter electrode to provide Li, with a commercial carbonate electrolyte of 1 M $LiPF_6$ in ethylene carbonate/dimethyl carbonate (EC/DMC). Li was deposited at a current density of 1 mA $cm^{-2}$ for 0.5 hours. After rinsing the samples three times in DMC, the Cu grid with grown Li dendrites was transferred from a glovebox to a focused ion beam (FIB)–SEM (FEI Helios NanoLab 660 DualBeam system) using a custom transfer box (*15*). The as-prepared Li dendrites were suspended on the Cu grid mesh as shown in Fig. 1B, with diameters ranging from ~100 to ~1000 nm (fig. S1).

Figure 1, C and D, shows the transfer of Li dendrite samples from the Cu grid to the microelectromechanical system (MEMS) device for uniaxial tensile testing in the SEM. A tungsten (W) manipulator probe in the SEM was used to pick up a Li dendrite (fig. S2), which was secured to the probe through e-beam–induced deposition with platinum (Pt). The Li dendrite was then pulled out from the Cu grid and transferred to the MEMS device, where Pt was again used to fix it at both ends (Fig. 1E). Fiducial markers were placed near the Li dendrite sample for strain measurement by digital image correlation. No focused gallium (Ga) ions were involved during the entire transfer process to prevent the artifact of irradiation (*16*). Quantitative tensile tests were conducted using a Bruker PI85L in-SEM picoindentation system. The nanoindenter tip pushed the top beam of the device, converting the applied compressive force into a uniaxial tensile force on the sample (*17*).

## Mechanical properties of a Li dendrite

A quantitative tensile test of a single Li dendrite was conducted in the SEM, as shown in Fig. 2A. Li dendrites were reported to be unstable under

[1]Department of Materials Science and Nanoengineering and the Rice Advanced Materials Institute, Rice University, Houston, TX, USA. [2]George W. Woodruff School of Mechanical Engineering, Georgia Institute of Technology, Atlanta, GA, USA. [3]Department of Mechanical and Industrial Engineering, New Jersey Institute of Technology, Newark, NJ, USA. [4]Shared Equipment Authority, Rice University, Houston, TX, USA. [5]Department of Electrical and Computer Engineering and Texas Center for Superconductivity at the University of Houston (TcSUH), University of Houston, Houston, TX, USA. [6]Department of Electrical and Computer Engineering, Rice University, Houston, TX, USA. [7]Applied Physics Graduate Program, Smalley-Curl Institute, Rice University, Houston, TX, USA. [8]Institute of High Performance Computing (IHPC), Agency for Science, Technology and Research (A*STAR), Singapore , Singapore. [9]School of Mechanical and Aerospace Engineering, Nanyang Technological University (NTU), Singapore, Singapore. [10]Department of Chemistry, Rice University, 6100 Main Street, Houston, TX, USA. ***Corresponding author. Email: hg23@rice.edu (H.Gu.); yyao4@Central.UH.EDU (Y.Y.); ting.zhu@me.gatech.edu (T.Z.); gao.huajian@tsinghua.edu.cn (H.Ga.); jlou@rice.edu (J.L.)** †These authors contributed equally to this work. ‡Present address: Mechano-X Institute, Applied Mechanics Laboratory, Department of Engineering Mechanics, Tsinghua University, Beijing, China.

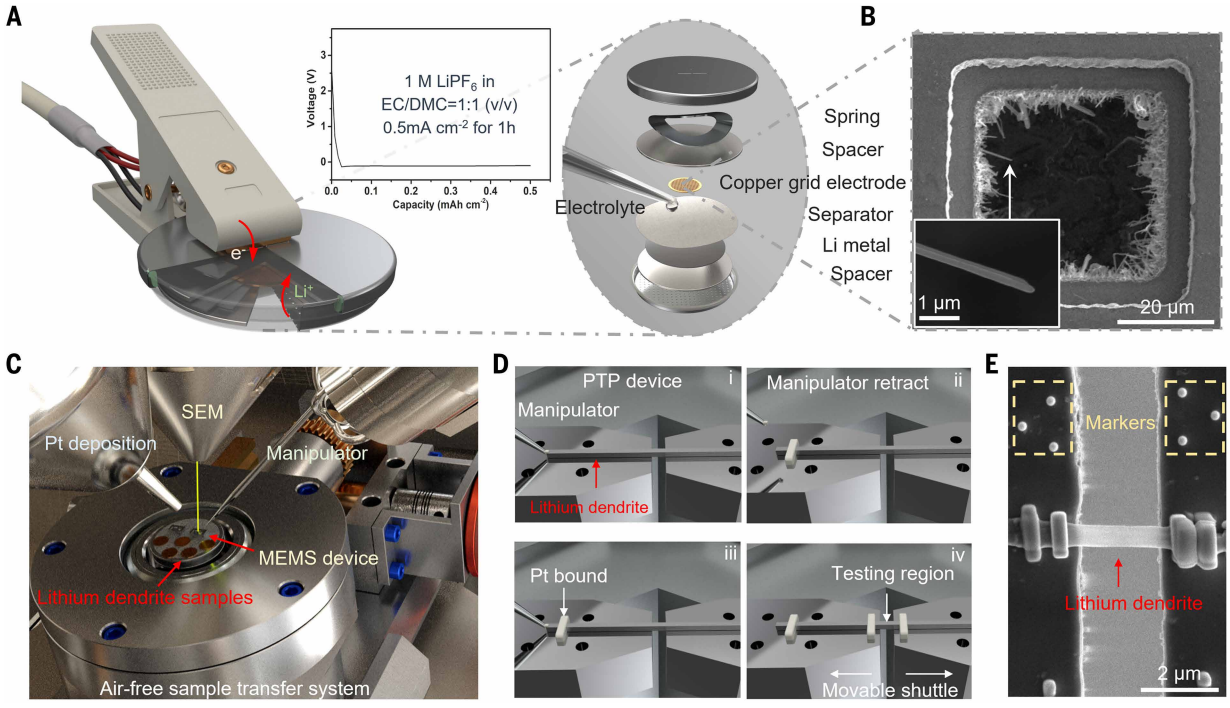


**Fig. 1. In situ SEM quantitative nanomechanical measurements on Li dendrites.** (**A**) (Left) Schematic illustration of Li dendrite preparation under realistic battery operation conditions. (Middle) Capacity-voltage profile of Li plating. (Right) Coin cell set-up for Li dendrite growth, with a Cu gird as the substrate. (**B**) Li dendrite growth on the Cu TEM grid. The inset shows the morphology of a typical Li dendrite. (**C**) Schematic illustration of the configuration in the SEM chamber for the Li dendrite transfer. (**D**) Schematic of in-SEM transfer of a Li dendrite from a Cu grid to a MEMS device for mechanical measurement. (**E**) SEM images show a representative Li dendrite sample after transfer, with fiducial markers deposited for strain measurement by digital image correlation.

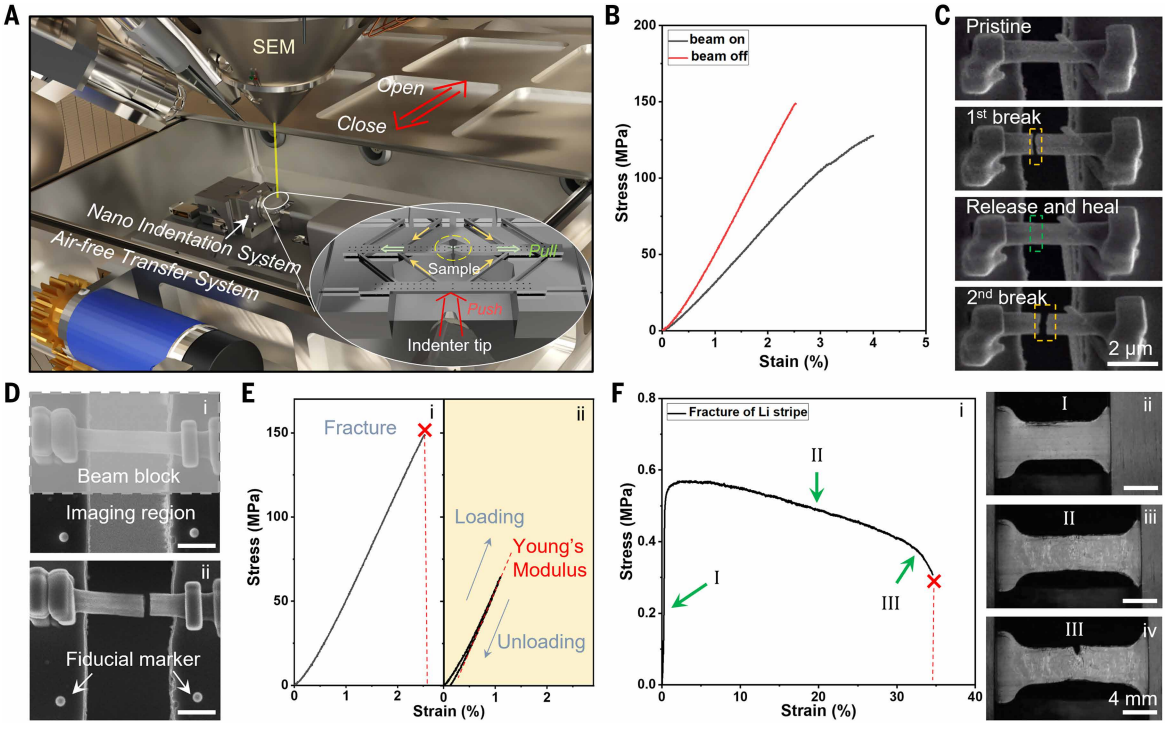


**Fig. 2. Mechanical properties of Li dendrites and bulk Li strips.** (**A**) Schematic illustration of a Li dendrite tensile test conducted in SEM. (**B**) Stress-strain curves of a Li dendrite with e-beam on and off during tensile testing. (**C**) SEM images display the e-beam healing effect on a Li dendrite. The first fracture was fully healed after e-beam treatment, whereas the second fracture occurred at a different location. (**D**) Typical tensile test of a Li dendrite; (i) and (ii) show the SEM snapshots of the Li dendrite before and after fracture. Scale bar, 1 μm. (**E**) Typical stress-strain curves of the fracture test and the loading and unloading test of Li dendrites, where the Young's modulus is derived from the unloading part. (**F**) Typical tensile test of a Li strip; (i) displays the typical stress-strain curve of the bulk Li strip, and (ii) to (iv) illustrate the optical snapshots of the Li strip at different stages, as indicated in (i).

an e-beam at room temperature owing to their low melting point and weak atomic bonding (*18*, *19*). Whereas e-beam damage to Li dendrites is well documented in TEM, e-beam effects on Li dendrites in SEM, which uses a lower-energy e-beam, remain unclear. During our in situ tensile tests, however, we observed substantial e-beam effects on the mechanical properties of Li dendrites. Figure 2B shows two tensile tests on the same Li dendrite, with and without e-beam, exhibiting different slopes (apparent modulus) in the loading curves. This result suggests a modulus change when the e-beam is applied. According to Fig. 2B, the apparent modulus with the e-beam off, $E'_{\text{beam-off}}$, was measured as ~6.51 GPa, within the same order of magnitude as previously reported values (*10*, *20*). The apparent modulus with the e-beam on, $E'_{\text{beam-on}}$, dropped to ~3.84 GPa. We also observed an e-beam healing effect on Li dendrites, as shown in Fig. 2C and fig. S8. We hypothesize that these observations may result from a temperature increase due to the e-beam thermal effect, which has been observed in Li and other metals (*18*, *21*–*23*). More details are provided in the supplementary materials. To avoid e-beam effects, Li dendrite samples were not exposed to the e-beam during tensile testing. Figure 2D shows a typical tensile test of Li dendrites, with displacement measured using fiducial marks on the device. Figure 2D, (i) and (ii), demonstrates the methodology for avoiding e-beam influence on Li dendrite properties and display the morphology of a typical Li dendrite before and after testing. The smooth fracture surface perpendicular to the loading axis, with no necking, also indicates brittle fracture. The stress-strain curve for the tested Li dendrite sample [Fig. 2E, (i)] demonstrates that its failure strength reached ~150 MPa, significantly higher than the yield stress of bulk Li metal (<1 MPa). The failure occurred immediately after the elastic region without visible plastic deformation, indicating brittle fracture behavior. For measurement accuracy, the Young's modulus was determined from the initial portion of the unloading curves [as illustrated in Fig. 2E, (ii)]. In situ tensile tests on Li dendrites with different diameters (ranging from 409 to 839 nm) showed a moderate variation in Young's modulus, ranging from 6.31 to 7.51 GPa, which is close to previously reported values (*10*, *24*). This is likely because the stiffer SEI coating occupies a larger volume fraction for dendrites with smaller diameters. All the tensile testing data are summarized in fig. S9. The Li dendrites in this study were grown in a coin cell under realistic conditions, ensuring that their structure and composition closely resemble those in practical battery cells.

To verify the generalizability of our findings, we conducted a qualitative tensile test of a Li dendrite grown within a sulfide SE using the manipulator in our FIB-SEM system. As shown in fig. S4A, the dendrite was grown in a Li | $Li_6PS_5Cl$ | Li symmetric cell without external stack pressure to intentionally induce contact loss and promote filament growth in poorly contacted regions. The as-grown Li dendrite (fig. S4B) was mounted by welding one end with Pt on the sample substrate and the other end to a W probe. The tensile test was performed by pulling the W probe (movie S1). The Li dendrite fractured at a strain of ~3.4% in a brittle manner. No necking or visible permanent elongation was observed during the test, which is consistent with the result of the dendrite shown in Fig. 2. In addition, operando SEM tests further confirmed this brittle fracture behavior in operating solid-state batteries (movie S2). During plating and stripping, Li dendrites experienced tension and compression loading and exhibited clear brittle fracture characteristics, as shown in fig. S6. These results show that Li dendrites fracture in a brittle manner under mechanical stress, losing electrical contact and forming dead Li, directly linking their limited plasticity to the degradation in solid-state batteries through this mechanism.

For comparison, a tensile test on a 750-μm-thick Li strip was also performed using a microtensile tester (Deben MICROTEST tensile stage) in a glove box, as shown in Fig. 2F. A custom-made sample punch was used to prepare 6-mm-long dog bone–shaped samples. Figure 2F, (i), shows a typical engineering stress–strain curve of the bulk Li strip, with a yield stress of ~0.6 MPa and ~35% elongation, consistent with previous studies (*10*). The labels (I, II and III) in Fig. 2F (i) indicate the stress and strain levels in the optical images in Fig. 2F, (ii), (iii) and (iv). Figure 2F (ii) shows the optical image of the pristine bulk Li strip. Under tensile loading, the strip's width gradually decreased, as shown in Fig. 2F (iii), until a major crack formed, causing the sample to fail. Beyond ~25% elongation, crack propagation dominated, with minimal geometric changes elsewhere. The Li strip fractured at ~35% elongation, as shown in Fig. 2F (iv). Given the reported Young's modulus of polycrystalline Li metal (7.8 GPa), we estimated the elastic limit to be ~0.007%, consistent with values in the literature (*10*, *25*).

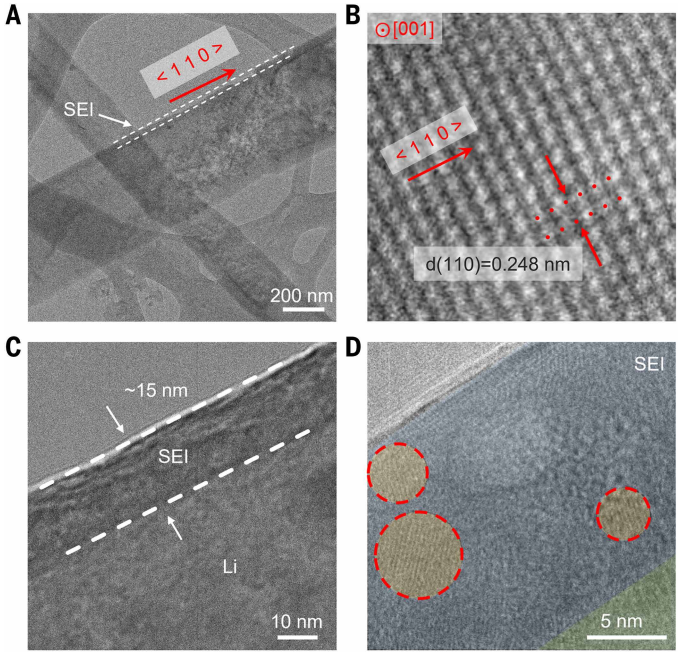


**Fig. 3. Cryo-TEM characterization of the core-shell structures of Li dendrites.** (**A**) TEM image of a Li dendrite growing along the <110>. (**B**) HRTEM image of the Li dendrite in (A), showing the Li lattice at atomic resolution. d, distance. (**C**) TEM image showing the thickness of a typical SEI. (**D**) HRTEM images of an SEI layer showing nanocrystalline domains.

## Cryo-TEM characterization of Li dendrites' core-shell structure

At the nanoscale, metallic materials generally exhibit higher failure strengths than their bulk counterparts, a phenomenon known as the mechanical size effect (*11*, *26*). To understand why Li dendrite samples endure much higher stress but lower strain than bulk Li, cryo-TEM was used to characterize the microstructure of as-grown Li dendrites and identify the critical features responsible for their brittleness and high failure strength (*19*). The bright-field TEM image in Fig. 3A shows that Li dendrites were coated with an SEI layer. High-resolution TEM (HRTEM) imaging confirmed that the Li dendrites are body-centered cubic single crystals with a growth direction of <110> (Fig. 3B) and an SEI thickness of ~15 nm (Fig. 3C). The detailed SEI structure observed through HRTEM aligns with the mosaic structure model by Peled *et al.*, where they suggested SEI as a heterogeneous mix of inorganic and organic components (*27*). In Fig. 3D, small crystalline domains (2 to 5 nm in size, marked by red circles) are dispersed within the amorphous SEI matrix. These grains likely represent the inorganic components of the SEI, whereas the amorphous matrix likely consists of organic components formed from carbonate electrolyte decomposition. Our findings on Li dendrite structure agree with those of previous studies, indicating that the Li dendrites prepared in this work

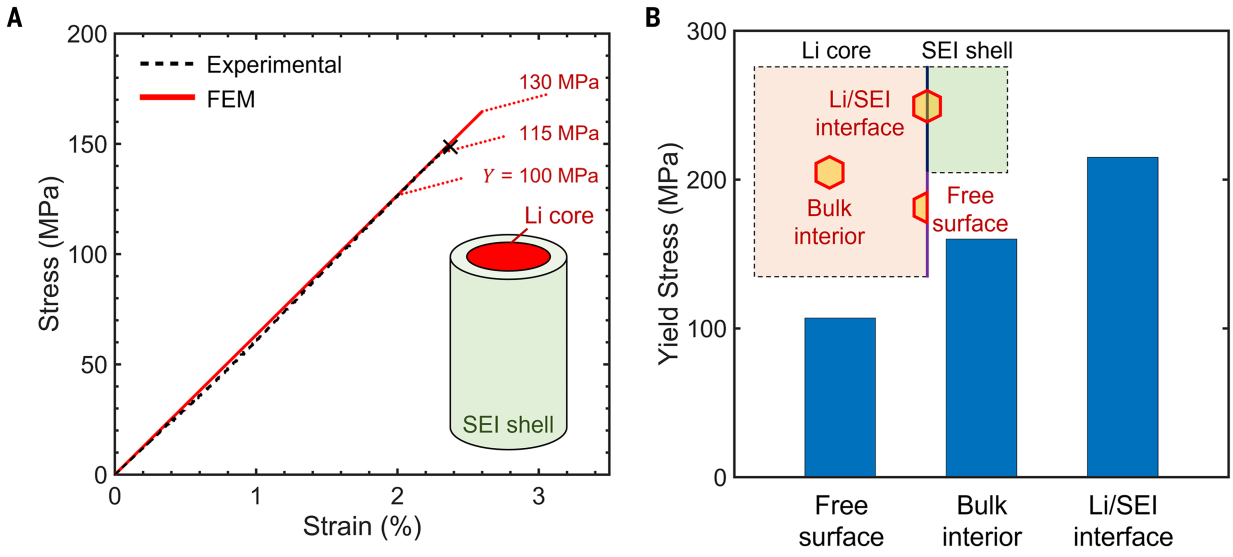


**Fig. 4. Finite element modeling and dislocation mechanics analysis of the brittle behavior of the Li dendrite.** (**A**) FEM predictions of the stress-strain curves of the Li dendrite under uniaxial tension as the yield stress of the Li core, *Y*, varies from 100 to 130 MPa. The FEM results (marked in red) align with the experimental data (black line) when *Y* exceeds 115 MPa, as the dendrite reaches the fracture stress (~150 MPa) before yielding (indicated by the onset of softening in red dashed lines). (**B**) The nucleation stress varies with the nucleation site, and the weakest site determines the yield stress of the Li core. In a bare Li dendrite, the free surface and the bulk interior are viable sites, with the former being the weakest. By contrast, in an SEI-coated Li dendrite, the free surface is replaced with the Li-SEI interface, and the bulk interior becomes the weakest site.

exhibit a typical composition and structure similar to those in practical Li-ion batteries (*19*, *28*).

## Finite element and dislocation mechanics analyses

The brittle behavior of Li dendrites is due to their core-shell structure with nanoscale cross-sections, as shown by finite element modeling and dislocation mechanics analysis. Using the finite element method (FEM), we simulated a cylindrical Li dendrite with an Li core (404 nm radius) and an SEI shell (15 nm thick), replicating the experimental tensile stress–strain curve (see Fig. 4A and the supplementary materials). Our results indicate that the yield stress of the Li core exceeds ~115 MPa, which is significantly higher than that of bulk Li (~0.6 MPa). This high yield strength is likely due to nanoscale strengthening of the Li core and the stiff SEI shell.

The pristine Li core, with its nanoscale cross-section, is dislocation starved, so plastic flow at ambient temperature is controlled by stress-driven, thermally activated dislocation nucleation. The yield stress is determined by the nucleation site with the lowest energy barrier (Fig. 4B). Using dislocation mechanics analysis (*29*–*32*), we estimated the energy barriers of dislocation nucleation at various sites: inside the Li dendrite, at the Li-SEI interface, and at the free surface (supplementary materials).

In a bare Li dendrite without an SEI shell, the weakest nucleation site is at the free surface, with an estimated yield stress of ~107 MPa. However, in an SEI-coated Li dendrite, the SEI layer increases the yield stress to ~160 MPa by replacing the free surface with a constrained Li-SEI interface, shifting the weakest site to the bulk interior. Our analysis excludes the weakening effect of stress-concentrating defects, which are expected to be minimal in Li dendrites with nanoscale cross-sections. Even after substantial dislocation nucleation, the SEI layer prevents dislocation from escaping, causing dislocation pile-up and back stress in the Li core (*33*). Given the nanoscale core size, this back stress is particularly high, resisting further dislocation nucleation and enhancing yield strength. Altogether, the nanoscale cross-section of the core-shell structure limits dislocation activities in the Li core, resulting in the observed brittle behavior of the Li dendrite.

Although our finite element and dislocation mechanics models assume an isotropic Li core and a homogeneous SEI coating, the above analyses remain applicable to real Li dendrites with compositional and structural complexity (see the supplementary materials for detailed discussion). Overall, the high strength and brittle fracture behavior of Li dendrites stem from the high yield stress of the Li core, which results from the suppression of dislocation activities owing to its nanoscale cross-section and the presence of a stiff SEI coating.

## Conclusions

In this work, we demonstrate the strong and brittle nature of Li dendrites, which arises from two key factors: (i) the small size and single-crystal structure of the Li core, which limits dislocation sources, and (ii) the presence of a stiff SEI coating, which suppresses dislocation nucleation and motion. These findings point to several unexplored failure mechanisms in Li-metal batteries. First, the formation of dead Li can result from fracture-induced fragmentation of Li dendrites during both plating and stripping owing to their brittleness, complementing the uneven electrochemical dissolution mechanism commonly observed during stripping (*34*, *35*). Second, the observed high strength of Li dendrites suggests alternative mechanisms for penetrating stiff SEs and separators. Third, the limited plasticity of Li dendrites may cause less conformal contact at the anode-electrolyte interface, thereby leading to increased interfacial impedance and nonuniform Li plating.

Our efforts to directly quantify the mechanical properties of Li dendrites provide insights into the design of solid-state batteries. First, because the strong and brittle behavior of Li dendrites is closely linked to the suppressed dislocation activities in the Li core, a potential strategy to mitigate fracture-induced fragmentation and dead Li formation is to use Li alloy anodes. This may provide abundant dislocation nucleation sources, facilitating plastic deformation in the Li core and making Li dendrites less prone to brittle fracture. This alloying strategy is also currently being explored in various other contexts (*36*–*38*). Second, the high strength and brittleness of Li dendrites suggest that they may behave like an elastic and brittle wedge when penetrating the SE, similar to the wedge-opening model (*39*–*41*). Thus, the contact

morphology between the Li dendrite and crack surfaces may influence crack growth in the SE and the stress distribution within the Li dendrite. Because cracks in SEs tend to conform to grain boundaries (*42*, *43*), the solid electrolyte microstructure may affect both electrolyte cracking and dendrite fracture. In short, tailoring the microstructure of SEs may be a viable approach to mitigate battery failure (*44*).

We developed an air-free approach to systematically measure the mechanical properties of individual Li dendrites, enabling direct study of their elastic and fracture behavior under uniaxial tension. Comparing bulk Li and Li dendrites, we found substantial differences in mechanical properties, particularly in fracture strength and mode. Unlike ductile bulk Li, Li dendrites fracture in a brittle manner with minimal plastic deformation under tensile stress. Understanding this brittle fracture behavior provides insights for suppressing dead Li formation and electrolyte cracking, enabling safer and more reliable Li-metal batteries.

## REFERENCES AND NOTES


1. K. N. Wood, M. Noked, N. P. Dasgupta, *ACS Energy Lett.* **2**, 664–672 (2017).
2. T. Krauskopf, F. H. Richter, W. G. Zeier, J. Janek, *Chem. Rev.* **120**, 7745–7794 (2020).
3. G. Rong *et al.*, *Adv. Mater.* **29**, 1606187 (2017).
4. C. Fang, X. Wang, Y. S. Meng, *Trends Chem.* **1**, 152–158 (2019).
5. C. Monroe, J. Newman, *J. Electrochem. Soc.* **152**, A396 (2005).
6. B. Kinzer *et al.*, *Matter* **4**, 1947–1961 (2021).
7. L. Porz *et al.*, *Adv. Energy Mater.* **7**, 1701003 (2017).
8. S. Yu *et al.*, *Chem. Mater.* **28**, 197–206 (2016).
9. F. P. McGrogan *et al.*, *Adv. Energy Mater.* **7**, 1602011 (2017).
10. A. Masias, N. Felten, R. Garcia-Mendez, J. Wolfenstine, J. Sakamoto, *J. Mater. Sci.* **54**, 2585–2600 (2019).
11. C. Xu, Z. Ahmad, A. Aryanfar, V. Viswanathan, J. R. Greer, *Proc. Natl. Acad. Sci. U.S.A.* **114**, 57–61 (2017).
12. Y. He *et al.*, *Nat. Nanotechnol.* **14**, 1042–1047 (2019).
13. L. Zhang *et al.*, *Nat. Nanotechnol.* **15**, 94–98 (2020).
14. B. Han *et al.*, *Adv. Mater.* **33**, 2100404 (2021).
15. Q. Ai *et al.*, *ACS Energy Lett.* **8**, 1107–1113 (2023).
16. J. Z. Lee *et al.*, *ACS Energy Lett.* **4**, 489–493 (2019).
17. Y. Yang *et al.*, *Nature* **594**, 57–61 (2021).
18. R. F. Egerton, P. Li, M. Malac, *Micron* **35**, 399–409 (2004).
19. Y. Li *et al.*, *Science* **358**, 506–510 (2017).
20. E. Darnbrough, J. Aspinall, M. Pasta, D. E. J. Armstrong, *Mater. Des.* **233**, 112200 (2023).
21. P. Yuan *et al.*, *Nano Lett.* **20**, 3019–3029 (2020).
22. Z. Hong, V. Viswanathan, *ACS Energy Lett.* **4**, 1012–1019 (2019).
23. Y. P. Varshni, *Phys. Rev., B, Solid State* **2**, 3952–3958 (1970).
24. T. Slotwinski, J. Trivisonno, *J. Phys. Chem. Solids* **30**, 1276–1278 (1969).
25. S. Tariq *et al.*, *Proceedings of the 2003 Particle Accelerator Conference*, Portland, OR, 12 to 16 May 2003. (IEEE, 2003), pp. 1452–1454.
26. A. T. Jennings *et al.*, *Acta Mater.* **61**, 2244–2259 (2013).
27. E. Peled, S. Menkin, *J. Electrochem. Soc.* **164**, A1703–A1719 (2017).
28. R. Lin *et al.*, *Nat. Nanotechnol.* **17**, 768–776 (2022).
29. V. A. Lubarda, J. A. Blume, A. Needleman, *Acta Metall. Mater.* **41**, 625–642 (1993).
30. E. Van der Giessen, A. Needleman, *Model. Simul. Mater. Sci. Eng.* **3**, 689–735 (1995).
31. J. P. Hirth, J. Lothe, T. Mura, *J. Appl. Mech.* **50**, 476-477 (1983).
32. C. D. van der Wekken, E. A. H. Vollebregt, *Math. Mech. Solids* **24**, 3537–3553 (2019).
33. Y. Zhang *et al.*, *Acta Mater.* **237**, 118155 (2022).
34. C. Wang *et al.*, *Adv. Mater.* **35**, e2209091 (2023).
35. K. Liang *et al.*, *Energy Environ. Sci.* **18**, 8487–8498 (2025).
36. T. Krauskopf, B. Mogwitz, C. Rosenbach, W. C. Zeier, J. Janek, *Adv. Energy Mater.* **9**, 1902568 (2019).
37. J. Aspinall *et al.*, *Nat. Commun.* **15**, 4511 (2024).
38. J. Cao *et al.*, *Nat. Commun.* **15**, 1354 (2024).
39. S. S. Shishvan, N. A. Fleck, R. M. McMeeking, V. S. Deshpande, *J. Power Sources* **456**, 227989 (2020).
40. Z. Ning *et al.*, *Nature* **618**, 287–293 (2023).
41. V. S. Deshpande, R. M. McMeeking, *Appl. Mech. Rev.* **75**, 010801 (2023).
42. S. Hao *et al.*, *Adv. Funct. Mater.* **31**, 2007564 (2021).
43. B. Zhang *et al.*, *Nat. Commun.* **16**, 1906 (2025).
44. S. Kalnaus, N. J. Dudney, A. S. Westover, E. Herbert, S. Hackney, *Science* **381**, eabg5998 (2023).


## ACKNOWLEDGMENTS

**Funding:** This work was supported by the US Department of Energy's Office of Energy Efficiency and Renewable Energy (EERE) under contract DE-EE0008864 and the Welch Foundation grants C-1716 and C-2248. This work was conducted in part using resources of the Shared Equipment Authority at Rice University. B.S. and Y.H. acknowledge the support from NSF (CMMI–2239545) and Welch Foundation (C-2065). B. Z., Hua G., and J. L. acknowledge the support from US Department of Energy's Office of Basic Energy Sciences under Contract DE-SC0018193. **Author contributions:** Conceptualization: Q.A., B.Z., H.Gu., J.L; Methodology: Q.A., B.Z., X.L., B.S., W.G., G.G., L.Z., X.W., Q.F., T.Z., D.S., F.W., X.T., H.Gu., Y.Zha., X.Z., Y.H., Y.Y., T.Z., H.Ga., J.L.; Investigation: Q.A., B.Z., X.L., L.Z., X.W., Y. Zhu, Y.L., F.W., X.T., H.Gu., Y.H., M.T., Y.Y., T.Z., H.Ga., J.L.; Visualization: B.Z., Q.A., X.L., L.Z., X.W., F.W., Y.Z.; Funding acquisition: J.L., Y.Y., Y.H.; Project administration: J.L.; Supervision: H.Gu., T.Z., H.Ga., J.L.; Writing – original draft: Q.A., B.Z., X.L.; Writing – review & editing: Q.A., B.Z., X.L., H.Gu., T.Z., H.Ga., J.L. **Competing interests:** Y.Y. has equity interests in LiBeyond, LLC, and Solid Design Instruments, LLC. The University of Houston reviewed and approved their relationship in compliance with its conflict-of-interest policy. **Data, code, and materials availability:** All data and materials are available in the main text or the supplementary materials. 

## SUPPLEMENTARY MATERIALS

science.org/doi/10.1126/science.adu9988
Materials and Methods; Supplementary Text; Figs. S1 to S13; References (*45*–*50*); Movies S1 and S2

Submitted 30 November 2024; accepted 16 January 2026

10.1126/science.adu9988

# Strong and brittle lithium dendrites

Qing Ai, Boyu Zhang, Xing Liu, Bongki Shin, Wenhua Guo, Guanhui Gao, Lihong Zhao, Xintong Weng, Qiyi Fang, Tianshu Zhai, Doug Steinbach, Yifan Zhu, Yifeng Liu, Fan Wang, Xiaoyin Tian, Hua Guo, Youtian Zhang, Xuan Zhao, Yimo Han, Ming Tang, Yan Yao, Ting Zhu, Huajian Gao, and Jun Lou

*Science* **391** (6790), . DOI: 10.1126/science.adu9988

**Editor's summary**

As a bulk material, lithium is a soft metal with the ability to deform, enabling good electrical contact to solid electrolyte surfaces. Ai *et al*. performed a nanomechanical study on lithium dendrites that grew on a copper transmission electron microscopy (TEM) grid in a working lithium-ion battery with liquid electrolytes. Lithium dendrites were transferred from the TEM grid to a testing device using an air-free procedure. Tensile tests performed in a scanning electron microscope showed that the dendrites have remarkably high fracture strength, high modulus, and brittle fracture. These observations may help to explain solid electrolyte penetration, poor interfacial contact, and the presence of "dead lithium" in solid-state batteries. —Marc S. Lavine